

Evaluation of IGRF-13 candidate models for epochs 2015.0 and 2020.0

C.C. Finlay and M.D. Hammer
DTU Space, Technical University of Denmark

Summary

Candidate models for DGRF-2015 and IGRF-2020 are compared with predictions of geomagnetic virtual observatory (GVO) time series, derived from *Swarm* satellite data, located at 300 uniformly distributed sites at 490 km altitude. In 2015.0 we find rms differences between the GVO time series and the DGRF candidate models of between 1.61 and 5.31 nT in B_r , 1.89 and 3.17 nT in B_θ , and 1.60 and 2.54 nT in B_ϕ . In comparison, the median of the candidate models shows rms residuals of 1.66 nT, 1.90 nT and 1.68 nT in B_r , B_θ , and B_ϕ respectively. Candidate G shows the largest rms differences compared to the GVOs in 2015.0. Extrapolating the GVO series, whose final point uses data up to 31st Oct 2019, forward to 2020.0, we find rms differences to the IGRF-2020 candidate models of between 3.07 and 9.60 nT in B_r , 4.31 and 6.46 nT in B_θ and 2.60 and 7.00 nT in B_ϕ , compared with 4.67 nT, 4.57 nT and 3.30 nT respectively for the median of candidate models. Candidate E, followed by B, show the largest differences compared to the GVO predictions for 2020.0. Based on these comparisons, we suggest to simply adopt the median of the candidate models for DGRF-2015 and IGRF-2020. We know of no reliable means for assessing SV candidate models so these were not evaluated.

1 Introduction

This note presents assessments carried out at DTU of DGRF-2015 and IGRF-2020 candidate models, based on comparisons with Geomagnetic Virtual Observatory (GVO) time series constructed from *Swarm* satellite data. These comparisons are complementary to the standard approach of evaluating IGRF candidate models based on statistical inter-comparisons between the models, and provides a test against localized estimates derived from satellite data. Our approach builds on previous work on GVOs [Mandea and Olsen, 2006, Olsen and Mandea, 2007, Whaler and Beggan, 2015] but we construct our estimates over 4 month intervals (designed to provide averaging over local time effects) on a global equal area grid of 300 points based on *Swarm* satellite data collected between 29th November 2013 and 31st October 2019. A similar approach has been used in recent secular variation and core flow studies [Hammer, 2018, Barrois et al., 2018, Kloss and Finlay, 2019]. Having obtained time series of the three components of the main field at each location, we fit cubic splines to each series individually and evaluate the resulting spline models in epochs 2015.0 and 2020.0 to enable direct comparisons with the submitted candidates models. We present examples of the GVO time series along with candidate model predictions, tables of rms residuals between the GVO predictions and the candidate models, and maps of residuals between the GVO predictions and each candidate model for the B_r , B_θ and B_ϕ components.

We follow P. Alken's proposed candidate model naming scheme: A=BGS, B=CEA-CSES, C=CU-NCEI, D=DTU, E=GFZ, F=IPGP, G=ISTERRE, H=IZMIRAN, I=JAPAN, J=LEEDS, K=MaxPlanck, L=NASA-GSFC, M=Potsdam-MaxPlanck, N= Spanish Team, O=Strasbourg. Of the candidate models, only model G used GVO data as input, although this was an earlier version of our GVO dataset running only to July 2019 and without any correction for the magnetospheric field applied. Candidates B, C, D, F, and N were derived from parent models that employed a CHAOS-type magnetospheric field model, which we also used in our processing scheme.

2 Geomagnetic virtual observatory time series

The GVO time series used here was derived from *Swarm* L1B Mag-L baseline 0505/0506 data collected between 29th November 2013 and 31st October 2019. We used three component vector field data from the three satellites *Swarm* Alpha, Bravo and Charlie. Data were decimated to a 15sec sampling rate and gross outliers deviating by more than 500 nT (in one or more vector component) from the CHAOS-7 field model were removed. Only data from dark regions (sun at least 10 degrees below the horizon) and satisfying geomagnetic quiet conditions ($Kp \leq 30$, $|dRC/dt| \leq 3$ nT/hr, and averaged over the previous two hours the merging electric field at the magnetopause $E_m \leq 0.8$ mV/m, $B_Z > 0$ nT and $|B_Y| \leq 10$ nT) are used. Estimates of the lithospheric field (from the LCS-1 model [Olsen et al., 2017], degrees 14 to 185) and the magnetospheric field (from the CHAOS-7 external field model, involving the hourly RC index derived from ground observatory data [Olsen et al., 2014]) were subtracted. Sums and differences of data along track (at 15 sec spacing) and in the east-west direction (between *Swarm* Alpha and Charlie) were constructed.

Based on the resulting sums and differences of *Swarm* data, GVO estimates were obtained as follows. A grid of 300 approximately equal area distributed points was first constructed at an altitude of 490 km above the Earth’s mean spherical reference radius. Then taking consecutive intervals of 4 months, all *Swarm* data sums and differences within 700 km of a target point were identified and used to determine a local Laplacian potential field model. The magnetic potential was expanded up to cubic terms and took the form

$$\begin{aligned}
 V(x, y, z) = & v_x x + v_y y + v_z z + v_{xx} x^2 + v_{yy} y^2 - (v_{xx} + v_{yy}) z^2 \\
 & + 2v_{xy} xy + 2v_{xz} xz + 2v_{yz} yz - (v_{xyy} + v_{xzz}) x^3 \\
 & + 3v_{xxy} x^2 y + 3v_{xxz} x^2 z + 3v_{xyy} x y^2 + 3v_{xzz} x z^2 + 6v_{xyz} x y z \\
 & - (v_{xxy} - v_{yzz}) y^3 + 3v_{yzz} y^2 z + 3v_{yzz} y z^2 - (v_{xxz} + v_{yyz}) z^3
 \end{aligned}$$

Data from Alpha and Charlie (except for east-west differences) were downweighted by a factor 2 and robust least squares estimation based on Huber weights was implemented. No estimate was produced if there were fewer than 30 data associated with a GVO location in a given 4 month window. Prior to fitting the potential the prediction of the IGRF-12 field model was removed from the data, this pre-whitening aids determination of the Huber weights. Once coefficients of the potential were been estimated, these were used to predict B_r , B_θ and B_ϕ at the GVO target point and the IGRF-12 prediction at this point was added back, undoing the pre-whitening. Any reasonable main field model can be used to perform the pre-whitening with little effect on the results [Hammer, 2018]. This procedure is repeated at all GVO grid points for all times to obtain a global set of GVO time series. Examples of these series are shown in Fig 1.

In order to compare with the candidate models in epochs 2015.0 and 2020.0 regularized (smoothing) cubic spline models were then fit to each GVO time series individually and the resulting spline models were evaluated in 2015.0 and 2020.0. The spline models were determined using a standard smoothing spline approach, by minimizing an objective function consisting of the sum squared residuals (between the GVOs and the spline fits) and a norm measuring the second time derivative of the spline model. After testing, the regularization parameter was fixed to a value of 100 in all cases. This was found to produce stable spline models that performed well for both the interpolation to 2015.0 and the extrapolation to 2020.0. Note that GVO 4 month estimates include data points centred on 1st Nov 2014 and 1st March 2015, two months either side of 2015.0, so it was possible to obtain high quality GVO estimates by spline interpolation to compare with the DGRF candidates in 2015.0. At the end of each series, the last 4 monthly GVO estimate was centred on 1st July 2019, based on data from 1st May 2019 to 31st August 2019. This left 2 months of data from 1st September 2019 to 31st October 2019, from these data we constructed final 2 month averaged GVO estimates, with allocated times of 1st October 2019. These two month estimates are the final data point shown in each time series of Fig 1; they may be slightly less reliable than the earlier 4 monthly averaged points, due to the smaller span of the contributing local times of the satellites, although we see little evidence of incompatibility with earlier trends. Examples of the cubic spline fits to the GVO series are shown in Fig 1.

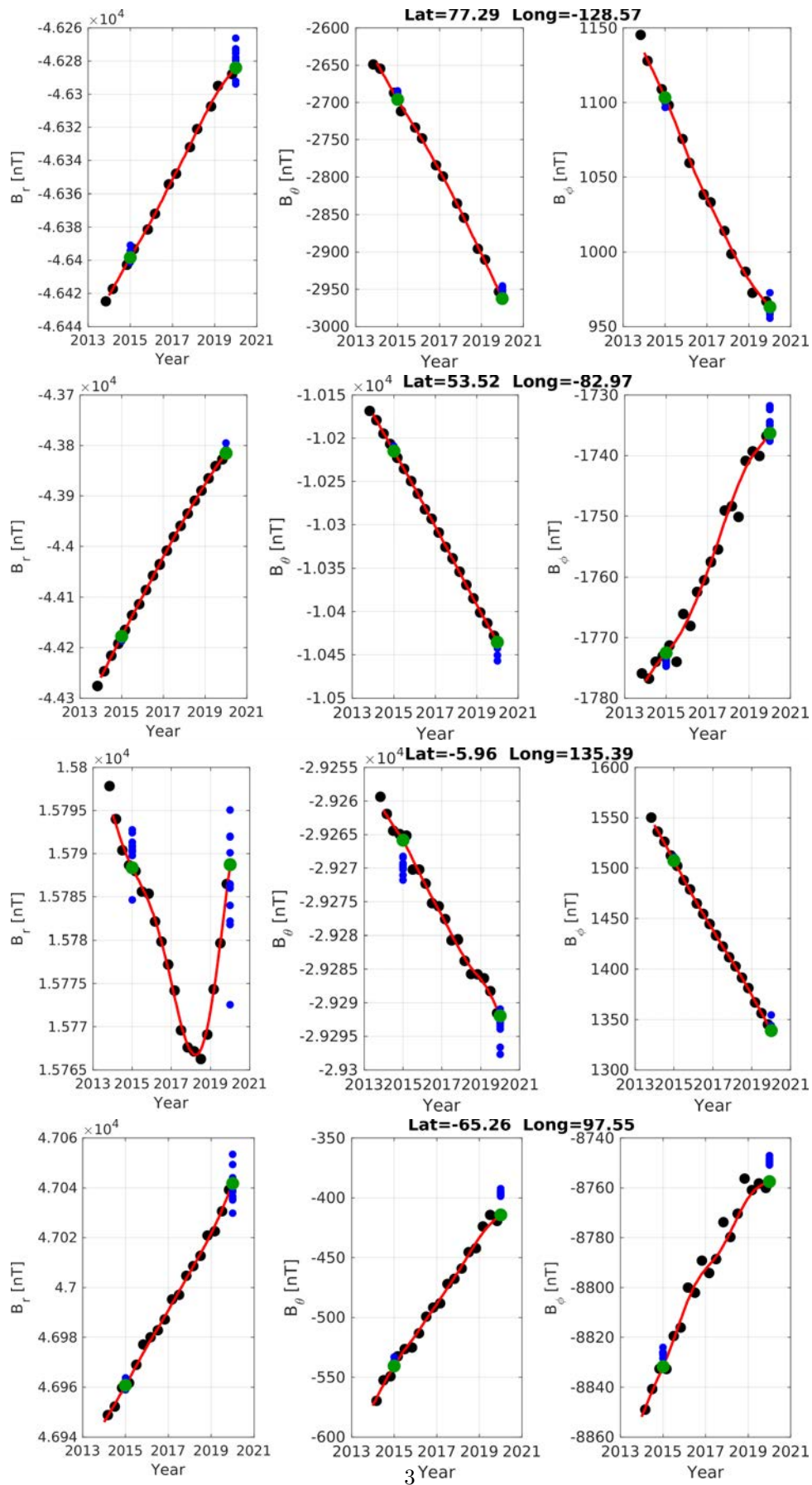


Figure 1: Example GVO time series, in the northern hemisphere (top two rows), and southern hemisphere (bottom two rows) showing example polar (top and bottom rows) and non-polar (middle two rows) locations. B_r in left column, B_θ in middle column, B_ϕ in right column. Black dots are the GVO estimates, red line is a cubic spline fit to each series, green dots are the spline fit predictions in 2015.0 and 2020.0. Blue dots are candidate model predictions in 2015.0 and 2020.0,

3 DGRF Epoch 2015 candidates

Considering time series such as those in Fig 1, the GVO predictions (green dots) in 2015.0 typically agree rather well with the DGRF candidate models (blue dots) with 10 out of 11 candidates having rms differences less than 3 nT. In Fig 1 the blue dots of the candidate models thus sometimes hidden behind the green dots of the GVO predictions. The median of the candidate models has rms differences to the GVO predictions of less than 2 nT in all components. Statistics of the comparisons between the GVO predictions and the candidate models are collected in Table 1, where there rms values are separated into values for non-polar and polar regions, where the polar region is defined as being poleward of 55 degree Quasi-Dipole latitude.

DGRF cand. model	A	C	D	E	F	G	H	L	M	N	O	Median Mod
rms B_r [nT]	1.88	1.89	1.61	2.18	1.65	5.31	3.05	3.05	1.84	1.99	3.00	1.66
rms B_θ [nT]	2.05	2.03	1.90	2.24	1.89	3.17	3.08	2.94	1.99	1.92	2.37	1.90
rms B_ϕ [nT]	1.80	1.71	1.66	1.75	1.66	2.54	2.27	1.81	1.66	1.60	2.21	1.68
mean of rms [nT]	1.91	1.88	1.72	2.06	1.73	3.67	2.80	2.60	1.83	1.84	2.53	1.75
rms non polar B_r [nT]	1.82	1.84	1.53	2.07	1.53	5.14	2.81	3.15	1.71	1.58	2.82	1.58
rms non polar B_θ [nT]	1.80	1.79	1.67	2.07	1.66	2.97	2.75	2.79	1.85	1.61	2.21	1.70
rms non polar B_ϕ [nT]	1.30	1.21	1.20	1.28	1.21	2.37	1.66	1.32	1.23	1.19	1.82	1.20
mean of rms non polar [nT]	1.64	1.62	1.47	1.81	1.46	3.50	2.41	2.42	1.60	1.46	2.28	1.49
rms polar B_r [nT]	2.13	2.12	1.94	2.66	2.09	6.02	3.98	2.57	2.33	3.29	3.75	1.99
rms polar B_θ [nT]	2.97	2.92	2.72	2.93	2.74	4.01	4.36	3.58	2.55	3.02	3.05	2.67
rms polar B_ϕ [nT]	3.26	3.15	3.03	3.17	3.01	3.23	4.09	3.27	2.95	2.84	3.54	3.08
mean of rms polar [nT]	2.79	2.73	2.56	2.92	2.61	4.42	4.14	3.14	2.61	3.05	3.45	2.58

Table 1: DGRF candidate model rms residual statistics compared to GVO series, with cubic smoothing spline interpolation to 2015.0. Units nanotesla (nT).

From Table 1 it is evident that candidate G has slightly higher rms residuals than the other candidates, especially for B_r . Further insight is obtained by considering maps of the residuals between the GVO predictions in 2015.0 and the candidate models, as presented in Fig 2. Here the residuals for B_r from candidate G clearly stand out. They have the geographic pattern of the time derivative (i.e. secular variation) of the radial field, but with the opposite sign. Since Fig 2 shows candidate model predictions minus GVO predictions, this means candidate G predicts field change of the same pattern, but lower amplitude than the GVOs (and the other candidate models, since these agree well with the GVO predictions). This is especially clear over North America. Candidate G is constructed in a different fashion from many of the other candidates, as it is based on a parent model that seeks to model the field over the past 180 years. This requires some compromises in order to handle sparser historical data, in particular a two year spline knot spacing is employed with the consequence that high frequency (less than 2-3 year) fluctuations in the SV are not well captured. This likely explains the differences in the predictions of candidate G compared to the other candidates (pers. comm. N. Gillet).

Aside from the higher amplitude residuals for candidate G in B_r , the residual patterns for the other candidates are broadly similar. Candidate H shows some zonal structure in its residuals for B_r and B_θ . Candidate L shows the residual patterns in B_r and B_θ expected due to its different treatment of the induced ionospheric field (this mainly affects g_1^0 g_3^0 , see [Olsen et al., 2005], Table 1 and Fig 4). Recomputing the GVO estimates after removing the predictions of the CM4 ionospheric plus induced field model, the rms residual in B_r for candidate L reduces from 3.05 nT to 1.80 nT, while the rms residual in B_θ reduces from 2.94 nT to 2.30 nT.

Compared to the GVO predictions in 2015.0, the ranking by rms residuals (averaging the rms values for B_r , B_θ and B_ϕ) of the candidates, starting with lowest residuals first, is D, F, M, N, C, A, E, O, L, H, G. Only D and F have smaller rms residuals than the median model. Based on this, a reasonable way to produce the final DGRF-2015, could be to simply adopt the median candidate model.

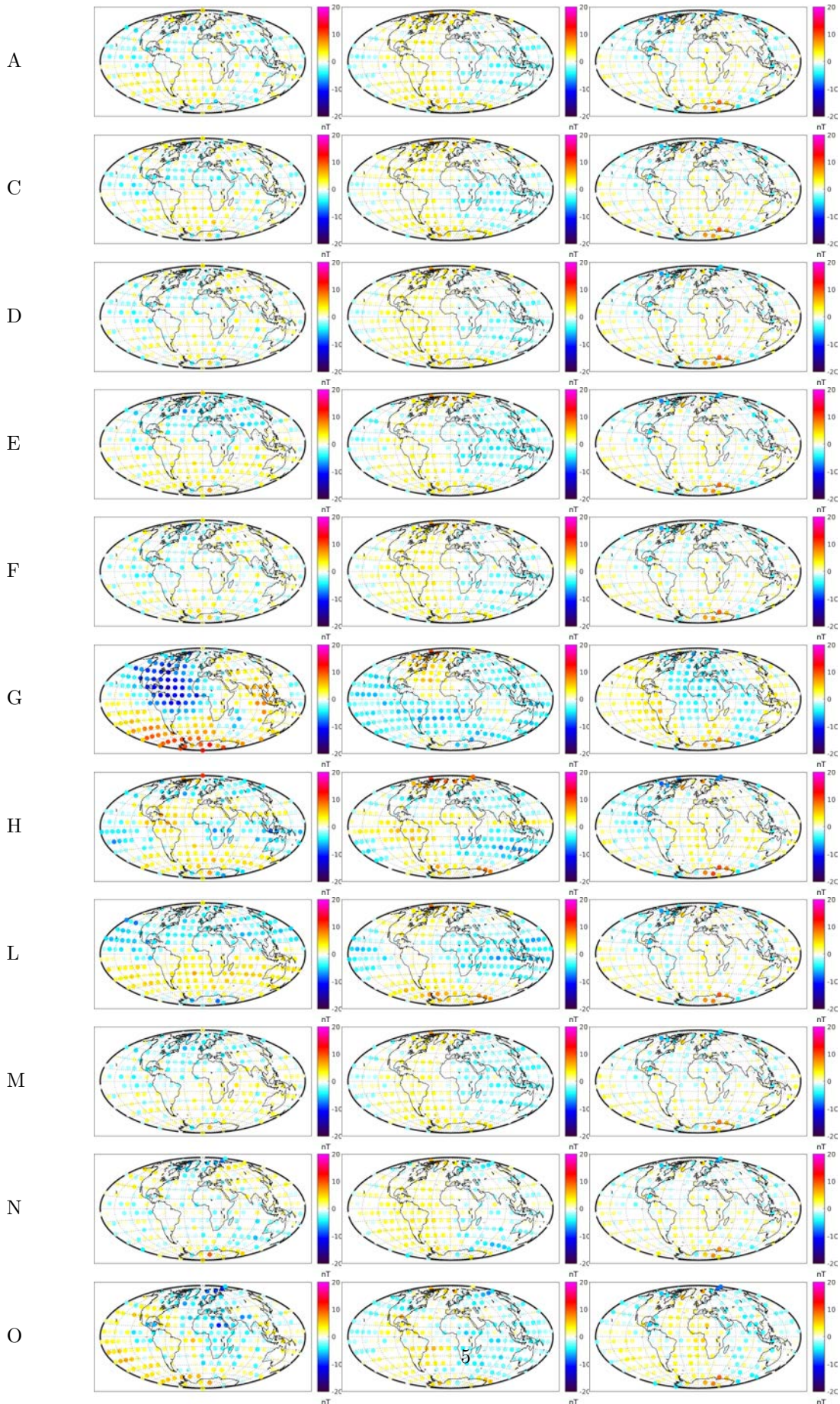


Figure 2: Residuals in nT, DGRF-2015 candidate model predictions in 2015.0 minus GVO series predictions, with spline interpolation to 2015.0. Hammer-Aitoff projection, colourbar +/- 20 nT.

4 IGRF Epoch 2020 candidates

The rms residuals between the predictions of the GVO series extrapolated to 2020.0 and the IGRF-2020 candidates models are higher than the comparable numbers for the DGRF in 2015.0. This is expected because extrapolation is needed, and magnetospheric models are typically less reliable for the final months due to delays with ground observatory data. Nonetheless, the comparisons are informative.

10 out of 12 candidates have rms differences (averaged over the three components) to the GVO prediction for 2020.0 less than 6 nT. This compares with 4.18 nT for the median candidate model. This can be compared with the differences found between published IGRF models (which require extrapolation) and later retrospective DGRF models; for example the rms vector field difference between the IGRF-10 model adopted for epoch 2005, and the DGRF model constructed retrospectively in 2010 was 12 nT. Statistics of the comparisons between the GVO predictions and the candidate models in 2020.0 are collected in Table 2.

IGRF cand. model	A	B	C	D	E	F	G	H	L	M	N	O	Median Mod
rms B_r [nT]	5.70	8.34	6.06	5.06	9.60	5.65	3.07	6.28	6.64	4.65	5.47	7.45	4.67
rms B_θ [nT]	4.89	6.46	5.90	4.61	5.94	4.89	4.31	5.07	5.78	4.54	5.29	5.96	4.57
rms B_ϕ [nT]	3.94	4.89	3.81	3.52	7.00	3.62	2.60	4.24	4.04	3.17	3.14	4.12	3.30
mean of rms [nT]	4.85	6.57	5.26	4.39	7.51	4.72	3.33	5.20	5.48	4.12	4.63	5.84	4.18
rms non polar B_r [nT]	5.47	8.10	5.40	4.79	10.10	5.33	2.64	6.34	6.77	4.33	4.71	6.41	4.50
rms non polar B_θ [nT]	3.07	5.30	3.70	2.66	4.84	2.93	2.81	3.22	4.74	2.50	3.22	5.14	2.64
rms non polar B_ϕ [nT]	3.53	4.52	3.33	3.14	7.14	3.22	1.94	4.12	3.70	2.81	2.86	3.89	2.94
mean of rms non polar [nT]	4.02	5.97	4.14	3.53	7.36	3.83	2.46	4.56	5.07	3.21	3.60	5.15	3.36
rms polar B_r [nT]	6.67	9.39	8.48	6.15	6.81	6.95	4.55	5.99	5.96	5.91	8.14	11.06	5.40
rms polar B_θ [nT]	9.91	10.62	11.93	9.66	9.81	10.09	8.55	10.18	9.48	9.68	10.85	9.11	9.59
rms polar B_ϕ [nT]	5.63	6.54	5.68	5.05	6.45	5.26	4.73	4.92	5.49	4.62	4.34	5.19	4.76
mean of rms polar [nT]	7.41	8.85	8.70	6.95	7.69	7.43	5.94	7.03	6.97	6.73	7.77	8.45	6.58

Table 2: IGRF candidate model rms residual statistics compared to GVO series, with cubic smoothing spline extrapolation to 2020.0. Units nanotesla (nT).

The rms residuals for candidates E and B are noticeable higher than for the other candidates, while the residuals for candidate G are noticeably lower. Maps of the residuals between the GVO series predictions in 2020.0 and the respective candidate model predictions, are presented in Fig. 3. The residuals for candidate E are noticeably enhanced in the Pacific region. Similar patterns are seen across the residuals in all candidates, particularly in B_r where residuals (candidate predictions minus GVO predictions) are generally positive over north America and negative over Asia. This may indicate shortcomings in the GVO spline extrapolation to 2020.0. The good fit of candidate G to the GVO predictions is perhaps surprising as it showed larger differences than other candidates in 2015.0. Candidate G is however directly based on GVO data (albeit without magnetospheric corrections applied) and perhaps its inability to follow rapid fluctuations in secular variation results in an extrapolation more similar to that found using the GVO-based smoothing spline extrapolation to 2020.0.

Compared to the GVO predictions for 2020.0, the ranking by rms residuals (averaging the rms values for B_r , B_θ and B_ϕ) of the IGRF-2020 candidate models, starting with lowest residuals first, is G, M, D, N, F, A, H, C, L, O, B, E. Only candidates B and E have rms residuals over 6 nT. Only G and M have smaller rms residuals than the median model. Based on this, a possible way to produce the final IGRF, could be to simply adopt the median candidate model.

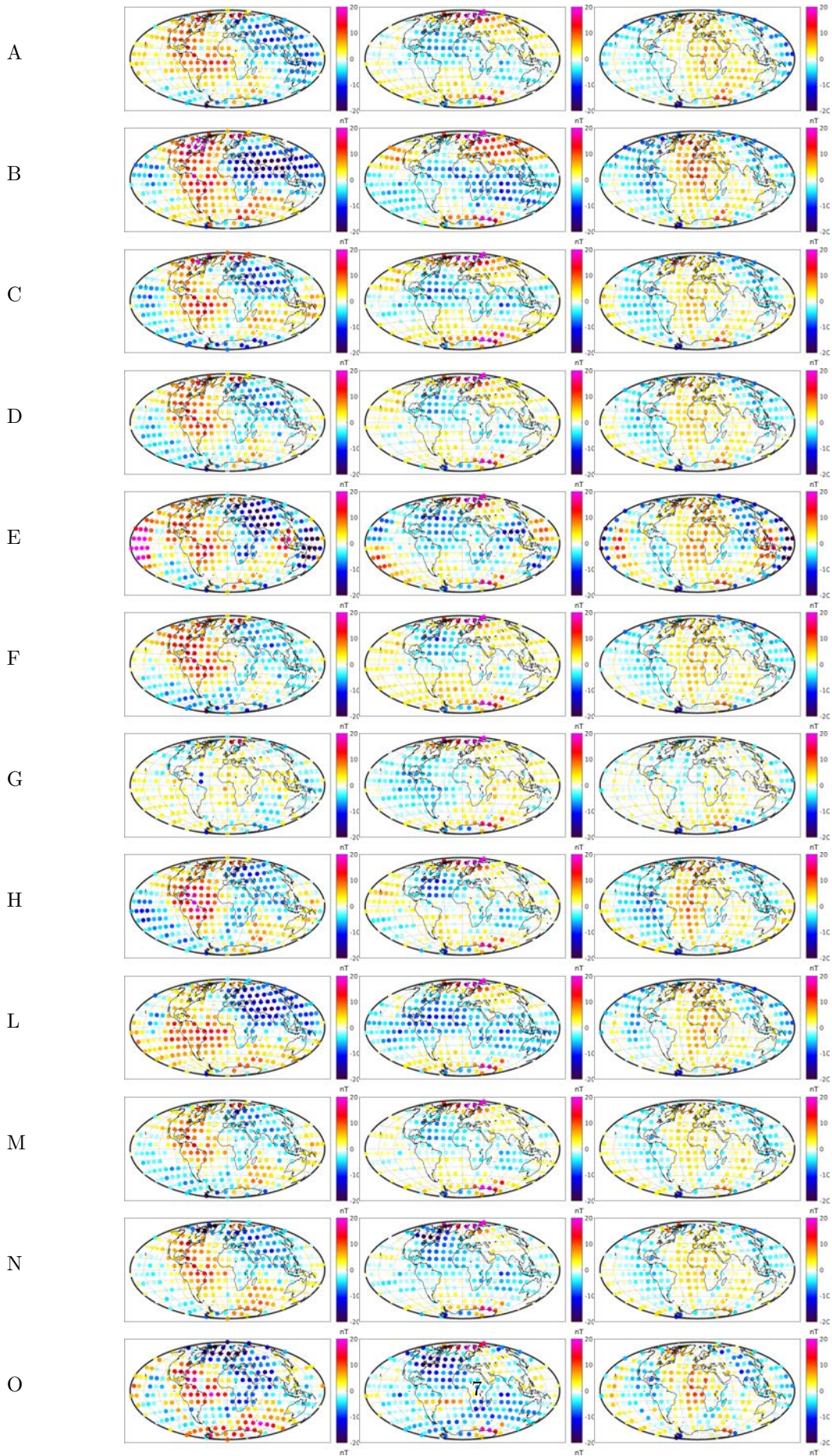


Figure 3: Residuals in nT, IGRF-2020 candidate model predictions in 2020.0 minus GVO series, with cubic smoothing spline extrapolation to 2020.0. Hammer-Aitoff projection, colourbar +/- 20 nT.

References

- Barrois, O., Hammer, M. D., Finlay, C. C., Martin, Y., and Gillet, N. (2018). Assimilation of ground and satellite magnetic measurements: inference of core surface magnetic and velocity field changes. *Geophysical Journal International*, 215:695–712.
- Hammer, M. D. (2018). *Local Estimation of the Earth’s Core Magnetic Field*. PhD thesis, Technical University of Denmark.
- Kloss, C. and Finlay, C. C. (2019). Time-dependent low-latitude core flow and geomagnetic field acceleration pulses. *Geophysical Journal International*, 217(1):140–168.
- Mandea, M. and Olsen, N. (2006). A new approach to directly determine the secular variation from magnetic satellite observations. *Geophysical research letters*, 33(15).
- Olsen, N., Lowes, F., and Sabaka, T. J. (2005). Ionospheric and induced field leakage in geomagnetic field models, and derivation of candidate models for DGRF 1995 and DGRF 2000. *Earth, Planets, Space*, 57:1191–1196.
- Olsen, N., Lühr, H., Finlay, C. C., Sabaka, T. J., Michaelis, I., Rauberg, J., and Tøffner-Clausen, L. (2014). The CHAOS-4 geomagnetic field model. *Geophysical Journal International*, 197(2):815–827.
- Olsen, N. and Mandea, M. (2007). Investigation of a secular variation impulse using satellite data: The 2003 geomagnetic jerk. *Earth and Planetary Science Letters*, 255(1):94–105.
- Olsen, N., Ravat, D., Finlay, C. C., and Kother, L. K. (2017). LCS-1: a high-resolution global model of the lithospheric magnetic field derived from CHAMP and Swarm satellite observations. *Geophysical Journal International*, 211(3):1461–1477.
- Whaler, K. A. and Beggan, C. D. (2015). Derivation and use of core surface flows for forecasting secular variation. *Journal of Geophysical Research: Solid Earth*, 120(3):1400–1414.